Journal of Magnetic Resonance 389 (2026) 108092

Contents lists available at ScienceDirect

Journal of Magnetic Resonance

journal homepage: www.elsevier.com/locate/jmr

Core–shell particles with tailored magnetic susceptibility for signal-efficient magnetic resonance imaging of granular systems

Stefan Benders [a,*], Jens P. Metzger [b,c], Mathieu Suter [c], Alice Dudle [c], Jenifer Nussbaum [c], Simon P. Gross [c], M. Raquel Serial [a,d], Christoph R. Müller [b], Klaas P. Pruessmann [c], Alexander Penn [a,b,c]

[a] Institute of Process Imaging, Hamburg University of Technology, Hamburg, Germany
[b] Department of Mechanical and Process Engineering, ETH Zurich, Zurich, Switzerland
[c] Institute for Biomedical Engineering, ETH Zurich and University of Zurich, Zurich, Switzerland
[d] Department of Process and Energy, Delft University of Technology, Delft, the Netherlands

ARTICLE INFO

Keywords:
MRI
NMR
Particles
Fluidized beds

ABSTRACT

Magnetic Resonance Imaging (MRI) has been recently applied to decipher the complex flow of dry granular materials, which play an important role in a variety of chemical engineering applications. In these materials, the short apparent transverse relaxation time of the constituent grains, T_2^*, leads to rapid signal decay and hence limits the choice of suitable pulse sequences. While oil-rich agricultural seeds and oil-filled core–shell particles containing substantial amounts of liquids have been used to generate MRI signals, these particles still suffer from T_2^* values much shorter than the transverse relaxation time T_2 of the contained liquid. This work investigates the effect of magnetic susceptibility on T_2^* through numerical simulations and experiments. Numerical results demonstrate that matching the magnetic susceptibility of the particles, χ_p, to that of the air between them, χ_{air}, reduces dipolar magnetic field inhomogeneities, theoretically enabling $T_2^* = T_2$. We also found that common imperfections in core–shell particles — such as asphericity, non-concentricity of core and shell, and uneven shell thickness — cause significant field inhomogeneities. These inhomogeneities can only be mitigated if both the core and shell materials have a magnetic susceptibility matching that of air. Based on these findings, we designed and manufactured core–shell particles with doped cyclooctane (CO) encapsulated in doped gelatin with $\chi_{core} \approx \chi_{shell} \approx \chi_{air}$. These particles exhibited a T_2^* of 3.85 ms, more than twice that of previously available materials, thus improving the signal-to-noise ratio and enhancing pulse sequence flexibility. This advancement opens up new possibilities for applications in engineering and the study of granular physics.

1. Introduction

MRI has long been an essential tool in clinical and biomedical applications. More recently, the utilization of MRI in chemical engineering applications has increased, since it allows for a non-intrusive observation of system parameters in complex three-dimensional reactors. These parameters include the spatial distribution of phases, flow patterns [1–3], temperature distributions [4–6] and chemical reactions [7]. While MRI is best suited to image liquids due to their favorable MR signal properties, recent advancements have expanded its application to more challenging systems, such as gases and even solids [8].

Solids generally have a low hydrogen content and experience rapid signal decay, which translates into a short apparent transversal relaxation time T_2^*. In these materials, T_2^* is often below one millisecond, making it challenging to obtain MRI signals using conventional MRI hardware. To address this, techniques such as ultrashort echo-time imaging (UTE imaging) [9] and zero-echo time imaging (ZTE imaging) [10] have extended applicability of MRI to solids [11]. Such methods often require long acquisition times, rendering them unsuitable for capturing transient flow phenomena such as particulate flow.

An alternative approach involves using solid materials that contain liquids, such as agricultural seeds (e.g. poppy and mustard seeds), which hold up to 40 vol.-% oil content [12]. The oil within these seeds is distributed in bodies of several micronmeters in diameter, resulting in longitudinal relaxation times (T_1) and transversal relaxation times (T_2) similar to that of the pure oils extracted from the seeds [13], with apparent transversal relaxation time T_2^* of ~1.5 ms [8]. Using such

* Corresponding author.
E-mail address: stefan.benders@tuhh.de (S. Benders).

https://doi.org/10.1016/j.jmr.2026.108092
Received 5 March 2026; Received in revised form 17 April 2026; Accepted 12 May 2026
Available online 19 May 2026

agricultural seeds, researchers have been able to probe the internal dynamics of granular systems, such as the spatial distribution of the solids as well as their time-averaged velocity, using time-efficient pulse sequences. These methods have been applied to fluidized beds [14,15], hopper flow [16], and particle convection in vibrated hoppers [17]. Additionally, core–shell capsules filled with liquids, such as vitamin E encapsulated in gelatin [18,19] have also been employed for similar purposes. More recently, Penn et al. [20] showed that using middle chain triglyceride (MCT) oil encapsulated in agar, the signal intensity, and the apparent transversal relaxation time of capsules is sufficient to enable time-efficient single-shot, echo-planar imaging readouts [21]. The methodology employs partial Fourier sampling [22], and parallel imaging [23] using radiofrequency receiver arrays that are conformal to the geometry of the studied system. The use of such time-efficient pulse sequences increased imaging speed considerably, allowing the direct observation of transient granular phenomena, including bubbling fluidization in fluidized beds [24] and dynamics of spouts in spouted beds [25,26].

Nonetheless, the values of T_2^* of these oil capsules, and even more so of agricultural seeds, is still more than one order of magnitude shorter than the theoretical maximum. This maximum corresponds to the intrinsic transversal relaxation time T_2 of the liquid within the pores of the particles or capsules. These short T_2^* values restrict the readout duration, limiting the k-space area that can be sampled within a single excitation shot, and ultimately constrain the achievable spatial resolution.

The root cause for these short T_2^* values in particle packings is the inhomogeneity of the static magnetic field ΔB_0, which arises from a mismatch in magnetic susceptibility (χ) between the diamagnetic particles and the slightly paramagnetic air between them. In the case of a single spherical capsule containing a single liquid core and a shell of uniform thickness, the magnetic field inside the core is homogeneous, independent of its magnetic susceptibility. Since the apparent transversal relaxation time (T_2^*) is directly related to differences in the magnetic field, it can be described by the simplified equation [27]:

$$\frac{1}{T_2^*} = \frac{1}{T_2} + \frac{\gamma}{2\pi}\Delta B_0, \tag{1}$$

where γ is the gyromagnetic ratio of the nucleus being measured and ΔB_0 is the magnetic field inhomogeneity. To reduce the inhomogeneity, the susceptibility of the material has to be matched as suggested by many examples in the literature [28–31]. Matching susceptibility of the particles to the surrounding air can reduce magnetic field inhomogeneity, allowing the apparent relaxation T_2^* to approach the intrinsic T_2 of the particles. This approach is particularly relevant in fluidized beds, in which ensemble effects can lead to local variations in magnetic susceptibility. Furthermore, the spectral properties of oil with multiple peaks in its NMR spectrum can cause undesired image artifacts such as ghosting or blurring.

In this work, dry core–shell capsules were developed which exhibit a significantly increased T_2^* and show a single peak in their NMR spectrum. By modifying the magnetic susceptibility of these capsules to match the surrounding air, the dipolar fields created around each particle were reduced, resulting in improved T_2^* values. Both the shell and the core were doped with rare earth compounds, to shift the magnetic susceptibility of the capsules towards the paramagnetic regime of the surrounding air.

2. Methods

2.1. Core–shell particles

The precursor solution of the shell was prepared by dissolving 300 g/l gelatin powder (Imagel BP, Gelita® Ag, Germany) in pure water which was doped with 3.15 wt.% of gadolinium-butrol (Gadovist 1.0 mmol/m injection solution, Bayer). After heating the solution under stirring to 90 °C, the solution was degassed. Next, the solution was cooled down to the encapsulation temperature of 50 °C. The encapsulator (BÜCHI B-390, Switzerland) was equipped with a pair of concentric nozzles with a core nozzle diameter d_{core} = 0.45 mm and a shell nozzle diameter d_{shell} = 0.9 mm. The cyclooctane (CO) core liquid was doped with 1.967 wt.% of tris(6,6,7,7,8,8,8-heptafluoro-2,2-dimethyl-3,5-octanedionato)dysprosium(III) (98+ % abcr GmbH, CAS 18323-98-3). Cyclooctane was chosen as a core material due to its similarity to commonly used oil, but single peak spectrum. This avoids chemical shift related artifacts in images. The flow rate of the shell precursor liquid was set to $\dot{V}$ = 600 ml/h using the built-in gas pressure-driven flow regulator, the flow rate of the core liquid was set to $\dot{V}$ = 400 ml/h using a syringe pump (Perfusor fm, B. Braun SE, Germany). The nozzle assembly was vertically vibrated using the built-in piezo shaker in order to break the liquid stream into droplets. The vibration frequency of the nozzle was set to 160 Hz at the start of each encapsulation batch and gradually lowered to 130 Hz in order to obtain a stable capsule stream throughout the batch. Capsules were collected in a magnetically stirred petroleum bath placed under the encapsulator (Fig. 1a). The petroleum bath was cooled to 1 °C using a jacketed beaker and a recirculating chiller in order to solidify the gelatine shell. After the encapsulation step, excess petroleum in the cooling bath was removed and the capsules were chemically crosslinked with glutaraldehyde. In order to dissolve the 50% aqueous solution of glutaraldehyde (CAS 111-30-8, Alfa Aesar) into petroleum, the glataraldehyde solution was mixed and shaken in equal proportions with toluene. Subsequently, the toluene enriched with glutaraldehyde was added to the petroleum bath containing the particles. Here, 15 ml of toluene was used for each 20 ml of cyclooctane and stirred at room temperature for 24 h. After crosslinking the shells, the particles were dried in a self-built rotary dryer, exposing them to a stream of dry air while rotating them. Subsequently, the particles were immersed into an ethanol bath 96 vol% to clean their surface from residual petroleum and to remove empty particles that float at the top of the bath due to their high buoyancy. The remaining particles were sieved to remove debris and particle clumps. The particle size distribution was measured optically with a camera and then evaluated by a script. The diameter was 1.27 ± 0.04 mm (Figure S1, Figure S2).

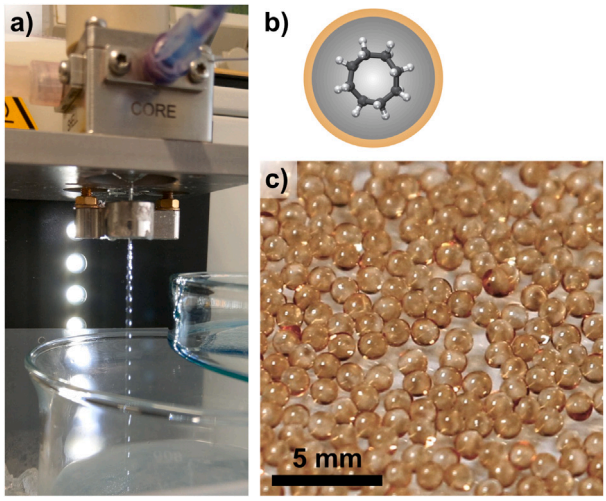

Fig. 1. Manufacture of MR signal source particles with tailored magnetic susceptibility. (**a**) Manufacturing of granular signal sources via a seamless encapsulation technique on a BÜCHI encapsulator B-390. (**b**) Schematic of the core–shell structure and (**c**) photograph of the particles.

2.2. NMR experiments

All magnetic resonance experiments in this work were conducted on a 3 T clinical MRI system (3T Achieva, Philips Healthcare, The

Netherlands). Magnetic susceptibility was measured using an MRI-based susceptometry device with a spherical volume of liquid placed around a sample vial containing the particles. The phase shift of an MRI image is measured and compared to the shift produced by an empty vial and one filled with pure water. Since the susceptibilty of air and water are known, the phase shift of the sample can be interpolated between these two values. More details on this susceptometry method are described in [31,32]. Free induction decays were measured in order to determine the $T_2{}^*$ of the particles. Fitting was performed assuming a monoexponential decay. The standard deviations of the $T_2{}^*$ values were calculated based on multiple measurements (three for seeds and oil-filled agar particles, six for doped cyclooctane particles). An additional uncertainty was added for the $T_2{}^*$ values of poppy seeds, mustard seeds and oil-filled agar particles, due to the fact that there was a slight uncertainty in the acquisition time of <1%. For gradient echo based images, the samples were placed in four cylinders next to each other. A gradient echo sequence with a variable echo time, a repetition time of 50 ms, a slice thickness of 10 mm and a resolution of $0.625 \times 0.625\,\mathrm{mm}^2$ was employed.

2.3. Numerical simulations

Simulations were performed with COMSOL Multiphysics 6 (Comsol Multiphysics, Sweden) using the magnetic fields, no currents module. The magnetic susceptibility of the gas (χ_{gas}) was set to 0.34 ppm, which corresponds to the magnetic susceptibility of air at ambient conditions [33]. The magnetic susceptibilities of the particle cores (χ_{core}) and shells (χ_{shell}) were varied while the external magnetic field was kept constant. The particles used in the simulations of the bed had a diameter of 1.27 mm and a shell thickness of 0.1 mm, matching the value of the particles engineered in this work. The three-dimensional particle packings were computationally created with Blender (Stichting Blender Foundation, The Netherlands) using the pbg-script [34,35]. A container diameter of 2.5 cm and a total number of particles of 100 was chosen. After generating the packing, all particles were resized to 98% of their original size while maintaining their spatial position in order to avoid problems with overlapping or too close meshes within COMSOL. The core and shell materials were assigned as empty materials with only the corresponding relative magnetic permeability $\mu_r = 1 + \chi_r$ set. The static magnetic field produced by the external magnetic field interacting with the particles was numerically simulated. The magnetic field was calculated everywhere. For the analysis, only the field inside the particles was analyzed, since only this signal contributes to the measured signal and T_2^*. A sufficiently big air sphere (15 mm for the bed) including a 5 mm infinite element domain on the outside was employed to ensure a proper simulation environment. A magnetic scalar potential of zero was applied to the edges of the air sphere improve numerical stability in the simulations. The background magnetic field was set to $3\,\mathrm{T}/\mu_0$ and relative permeabilities were used from the susceptibility of the material measured by susceptometry. Zero magnetic scalar potential ($V_{\mathrm{m}} = 0$) was applied to the sphere around the packing (Comsol "Zero Magnetic Scalar Potential"). Magnetic insulation ($\mathbf{n} \cdot \mathbf{B} = 0$) was applied to the infinite element domain around the sphere of air (Comsol "Magnetic Insulation") with flux conservation across all geometries.

3. Results

3.1. Numerical simulations

Numerical simulations were conducted to estimate the magnetic field inhomogeneity around single core–shell particles and packings of core–shell particles in a constant and homogeneous magnetic field (B_0). According to classic, electromagnetism theory [36], the static magnetic field inside a sphere of constant magnetic susceptibility χ_{i} exposed to a uniform external magnetic field $\mathbf{B}_0$ is constant and can be expressed by the following equation:

$$\mathbf{B}_{\mathrm{inside}} = \mathbf{B}_0 + \frac{2}{3}\mu_0\mathbf{M}, \tag{2}$$

with the magnetization of the sphere being

$$\mathbf{M} = \frac{3}{\mu_0}\left(\frac{\mu - \mu_0}{\mu + 2\mu_0}\right)\mathbf{B}_0, \tag{3}$$

and $\mu = \mu_0\mu_{\mathrm{r}}$ being the total magnetic permeability, $\mu_{\mathrm{r}} = (1 + \chi_{\mathrm{r}})$ the magnetic permeability of the material with a magnetic susceptibility χ_{r}, and μ_0 the vacuum permeability.

Moreover, the external field resembles that of a dipole. The analytical solution for the field inside the sphere holds also if the sphere is confined by a shell of uniform thickness, even if the magnetic susceptibility of the shell material χ_{S} differs from the susceptibility of the core material χ_{C}.

The magnetic susceptibility (χ_{P}) of such a core–shell particle can be described by the following volume-weighted sum of its constituent susceptibilities:

$$\chi_{\mathrm{P}} = \chi_{\mathrm{C}}\frac{V_{\mathrm{C}}}{V_{\mathrm{C}} + V_{\mathrm{S}}} + \chi_{\mathrm{S}}\frac{V_{\mathrm{S}}}{V_{\mathrm{C}} + V_{\mathrm{S}}} \tag{4}$$

where V_{C} and V_{S} are the respective volumes of the constituent materials. In order to achieve susceptibility matching between the particles and the air the following condition needs to be fulfilled

$$\chi_{\mathrm{P}} \overset{!}{=} \chi_{\mathrm{Air}}. \tag{5}$$

There are three possibilities to fulfill Eq. (5): (A) only the core material is doped while the susceptibility of the shell is left unaltered (Fig. 2, top right), (B) only the shell material is doped while the susceptibility of the core is left unaltered (Fig. 2, bottom left), or (C) both the core and the shell material are doped (Fig. 2, bottom right).

In case (A) the magnetic susceptibility of the core needs to be adjusted to match the following condition:

$$\chi_{\mathrm{C}} = \frac{V_{\mathrm{C}} + V_{\mathrm{S}}}{V_{\mathrm{C}}}\left(\chi_{\mathrm{Air}} - \chi_{\mathrm{S}}\frac{V_{\mathrm{S}}}{V_{\mathrm{C}} + V_{\mathrm{S}}}\right). \tag{6}$$

In case (B) the magnetic susceptibility of the shell needs to be adjusted to match the following condition:

$$\chi_{\mathrm{S}} = \frac{V_{\mathrm{C}} + V_{\mathrm{S}}}{V_{\mathrm{S}}}\left(\chi_{\mathrm{Air}} - \chi_{\mathrm{C}}\frac{V_{\mathrm{C}}}{V_{\mathrm{C}} + V_{\mathrm{S}}}\right) \tag{7}$$

In case (C) both the core and the shell materials are doped such that Eq. (5) is fulfilled. While it is possible to fulfill this condition with many combinations of χ_{C} and χ_{S} (represented by the yellow diagonal line in Fig. 3c), there are important practical advantages of matching both the core and the shell material to the susceptibility of air, which mathematically corresponds to the following condition:

$$\chi_{\mathrm{S}} = \chi_{\mathrm{C}} = \chi_P = \chi_{\mathrm{Air}}. \tag{8}$$

If Eq. (8) is fulfilled, the susceptibility match becomes robust against common manufacturing imperfections such as asphericity of the core and/or shell, and acentricity of particles and variations in the shell thickness that are difficult to avoid. This makes it easier to manufacture particles of homogeneous magnetic susceptibility matching that of air.

Numerical simulations of an undoped single particle ($\chi_{\mathrm{Core}} = -8.37\,\mathrm{ppm}$, $\chi_{\mathrm{Shell}} = -5.09\,\mathrm{ppm}$) surrounded by air ($\chi_{\mathrm{Air}} = 0.34\,\mathrm{ppm}$) in the main magnetic field show the analytically predicted dipolar shape (Fig. 2). The local field around the particle is lower along the main field direction and higher perpendicular to it. Matching the particle susceptibility to that of the surrounding medium (i.e. air), by doping (A) only the particle shell ($\chi_{\mathrm{Core}} = -8.37\,\mathrm{ppm}$, $\chi_{\mathrm{Shell}} = 13.3\,\mathrm{ppm}$), (B) doping only the core ($\chi_{\mathrm{Core}} = 3.99\,\mathrm{ppm}$, $\chi_{\mathrm{Shell}} = -5.09\,\mathrm{ppm}$), or (C) doping both core and shell ($\chi_{\mathrm{Core}} = 0.34\,\mathrm{ppm}$, $\chi_{\mathrm{Shell}} = 0.34\,\mathrm{ppm}$) to fulfill Eq. (4), results in no visible field patterns caused by the particle.

Effects of the susceptibility manifest strongly in ensembles of particles, such as in packed or fluidized beds. While a single particle

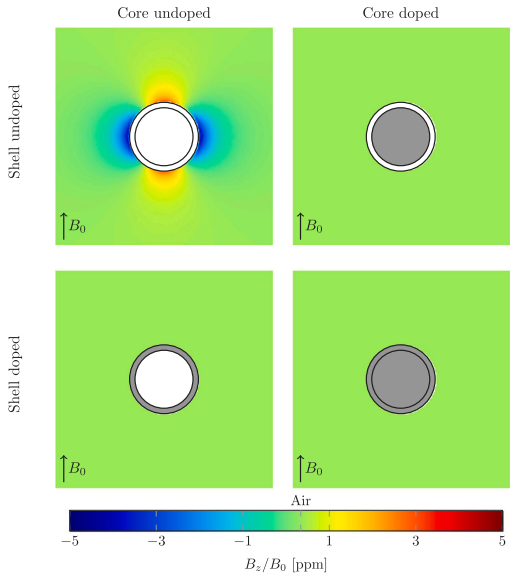

Fig. 2. Simulated magnetic field outside a core–shell particle for different doping scenarios if surrounded by air and exposed to a homogeneous static magnetic field $B_0 = 3\,\mathrm{T}$. Only the field outside the particle is shown. Inside the core the magnetic field is perfectly homogeneous as predicted by Maxwell's equations.

shows a clearly defined magnetic field pattern around the particle, an ensemble of particles creates a locally varying static magnetic field (Fig. 3a) within neighboring particles, which shortens T_2^* appreciably. This occurs because the magnetic fields produced by the individual particles influence the field within neighboring particles. By simulating the fields in a particle packing and analyzing the distribution of the magnetic field within the visible core material, an estimate for T_2^* in the inhomogeneity dominated regime can be obtained (Fig. 3c).

Matching the susceptibility of particles to the susceptibility of the air surrounding the particles reduces the inhomogeneities of the static magnetic field, which can be observed by a reduced width of the $\Delta B_z/B_0$ distribution shown in Fig. 3b, where the unmatched case is shown in gray and the matched case in red. In the matched case, the inhomogeneities of the static magnetic field become so low, that the second term on the right hand side of Eq. (1), becomes negligible and hence the theoretical limit $T_2^* = T_2$ can be achieved. Considering a T_2 of 30 ms, a T_2^*-value of 1.9 ms for the unmatched case is estimated by Eq. (1). On the contrary, T_2^* can reach the theoretical maximum of 30 ms (i.e. $T_2^* = T_2$) with perfect doping. This shows the potential of increasing signal lifetime by matching the particle susceptibility. Achieving susceptibility matching for spherical particles involves adjusting the susceptibility of the core and/or the shell. In Fig. 3c, a clear line of optimal matching can be identified, which corresponds to the matching calculated from the material volume fractions (Eq. (4)). The graph in Fig. 3c suggests the possibility of only matching one component, which would simplify manufacturing significantly. In experimental reality, manufacturing imperfections, such as off-centered cores, imperfect shapes or variations in shell thickness, make this approach less favorable. Some of these shapes are depicted in Fig. 4 with more cases in Figure S3 and Figure S4.

3.2. Experimental results

NMR free induction decays demonstrate the effect of particle susceptibility matching over conventional agricultural seeds and oil-filled agar particles (Table 1, Fig. 5). Oil-filled agar particles (1.62 ± 0.23 ms), mustard seeds (1.37 ± 0.18 ms) and poppy seeds (1.35 ± 0.21 ms) exhibit short signal lifetimes. Doping core–shell particles experimentally

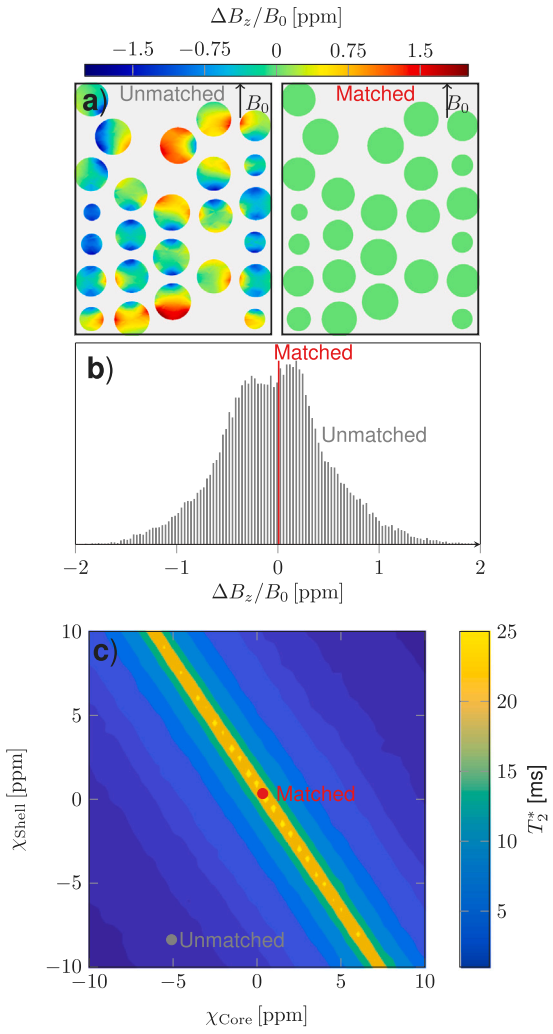

Fig. 3. (a) Magnetic field variations in an ensemble of particles. A central slice of the bed is shown, and therefore different particle cross-sections are observed. To increase clarity, the particle shells are not shown. Left: Unmatched particles with approximated susceptibilities for the core and shell ($\chi_{\mathrm{Core}} = -8.37$ ppm, $\chi_{\mathrm{Shell}} = -5.09$ ppm). Right: Matched particles with the susceptibility of air. The offset of the field with respect to the mean value over this slice (ΔB_z) is shown. (b) Histogram of the field deviation from the average field normalized by B_0 in a 3D bed. The FHWM of the unmatched particles is 1.01 ppm. (c) Numerical prediction of T_2^* employing an estimate of T_2 of 30 ms for a bed of particles of different susceptibility values. The diagonal of best homogeneity corresponds to Eq. (4).

leads to a T_2^* of 3.85 ± 0.23 ms. Since Dysprosium can also alter the T_2 of the bulk solvent, it sets a limit to the effectiveness of this method. The maximum achievable value of T_2^* is therefore lower than for pure solvent. Studies on other complexes in water indicate a strong dependence on field and chelates [39–41]. From the strongest relaxation agent described by Aime et al. a relaxation time of the order of 40 ms can be expected for water. While the complex used in this work is slightly different and the solvent is cyclooctane, the relevant times are similar and therefore this effect does not dominate. Future work can be done to optimize the chelation to reduce such effects further and to improve the encapsulation technique to reduce manufacturing imperfections. Furthermore, T_2^* is limited by the homogeneity of the magnet and therefore cannot reach the theoretical limit of T_2 in large-bore scanners. Nevertheless, the two-fold increase in T_2^* through doping significantly extends signal lifetime or increases signal intensity when using an identical echo time, respectively. For example, considering

Table 1
Mean NMR properties of the different particles used for MRI experiments. T_2^* was measured using a free induction decay (Fig. 5).

	Typical diameters [mm]	Shape	T_2^* [ms]
Poppy seeds	1 [37]	Kidney shaped	1.35 ± 0.21
Mustard seeds	1.5 (brown) [38] - 3 (yellow)	Spherical to ellipsoidal	1.37 ± 0.23
Oil-filled agar particles	1 and 3 [24]	Spherical	1.62 ± 0.18
Doped CO-particles	1.27	Spherical	3.84 ± 0.23

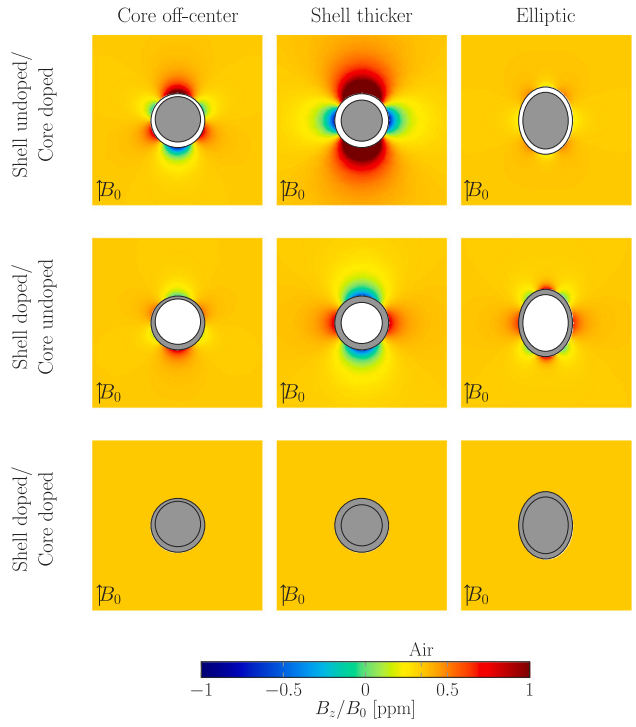

Fig. 4. Common manufacturing imperfections and their effect on magnetic field homogeneity for different materials doping conditions. The most common manufacturing imperfections are off-centered cores ($\Delta z = 0.025$ mm), altered shell-thickness (0.15 mm) and oval shape ($c = 1.25$). The field around the particles influences other particles in their vicinity and therefore will increase inhomogeneity.

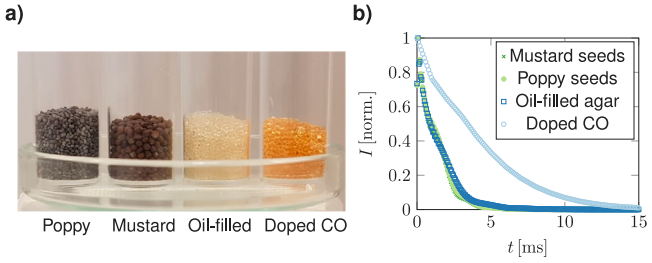

Fig. 5. (a) Image of the four particle types explored here. (b) Free induction decay for the different particle types evaluated in this paper. All data were interpolated.

oil-filled agar particles and doped core–shell particles with an imaging sequence with an echo time of 5 ms, the signal would be 4.68 times larger. The extended signal lifetime would also enable the use of longer echo times. This effect can be observed clearly when using gradient echoes with different echo times (Fig. 6). While the signal decays rapidly for oil-filled agar, mustard or poppy seed with close to no signal remaining at 7 ms echo time, the signal of the doped particles is still visible. These advantages will yield higher resolution images due to a higher number of readout points or increased velocity encoding resolution due to longer bipolar pulses. The long-term stability of these particles remains a subject of investigation as there is the possibility of leaching of dopants from the core material. This could lead to imperfect matching.

4. Conclusions

This work highlights the importance of matching the magnetic susceptibility of particles in MR imaging of granular materials in order to maximize signal quality and lifetime of ensembles of granular particles. Magnetic field simulations have shown that particle shape plays a significant role for matching. While for perfectly spherical particles, it is sufficient to either match the core or shell, for other shapes, the both core and shell have to be matched with shifting agents to obtain optimal T_2^*. In a first attempt, doped cyclooctane particles outperformed conventional particles in signal lifetime. These particles are challenging to manufacture in large quantities and doping with shifting agents is not trivial. One reason for choosing cyclooctane was its single-peak spectra avoiding chemical shift artifacts and its similarity to oil. A future focus will be the exploration of materials which are easier to manufacture and dope. Furthermore, there is a strong dependence of the field patterns on the shape of the particles. Therefore, manufacturing techniques should aim for particles of a high sphericity.

CRediT authorship contribution statement

Stefan Benders: Writing – review & editing, Writing – original draft, Visualization, Validation, Methodology, Investigation, Formal analysis, Data curation, Conceptualization. **Jens P. Metzger:** Writing – review & editing, Investigation. **Mathieu Suter:** Writing – review & editing, Investigation. **Alice Dudle:** Writing – review & editing, Methodology, Investigation. **Jenifer Nussbaum:** Writing – review & editing, Investigation. **Simon P. Gross:** Writing – review & editing, Methodology, Conceptualization. **M. Raquel Serial:** Writing – review & editing, Validation, Methodology, Investigation, Formal analysis, Data curation. **Christoph R. Müller:** Writing – review & editing, Supervision, Resources, Funding acquisition. **Klaas P. Pruessmann:** Writing – review & editing, Validation, Supervision, Resources, Methodology, Funding acquisition, Formal analysis, Conceptualization. **Alexander Penn:** Writing – review & editing, Writing – original draft, Validation, Supervision, Resources, Project administration, Methodology, Investigation, Funding acquisition, Formal analysis, Data curation, Conceptualization.

Declaration of competing interest

The authors declare that they have no known competing financial interests or personal relationships that could have appeared to influence the work reported in this paper.

Acknowledgments

The authors gratefully acknowledge the funding of this project by Deutsche Forschungsgemeinschaft (DFG, German Research Council) under project number 471615686.

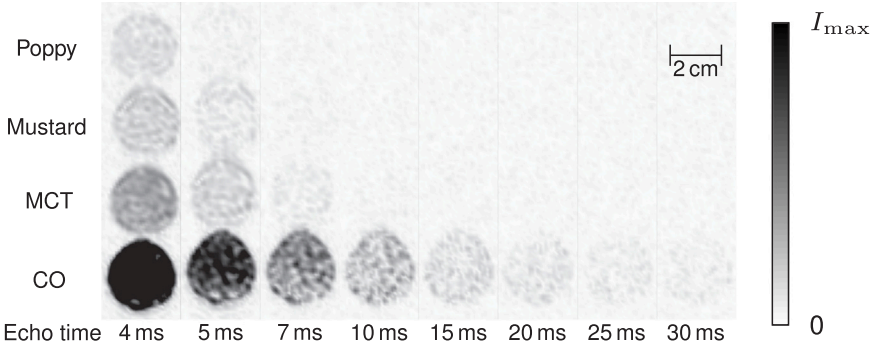

Fig. 6. Gradient echo images with different echo times for all particles. The particles were placed in four vials next to each other and the gradient echo sequences were performed with varying echo times.

Appendix A. Supplementary data

Supplementary material related to this article can be found online at https://doi.org/10.1016/j.jmr.2026.108092.

Data availability

Data will be made available on request.

References

[1] E. Fukushima, Nuclear Magnetic Resonance as a tool to study flow, Annu. Rev. Fluid Mech. 31 (Volume 31, 1999) (1999) 95–123, http://dx.doi.org/10.1146/annurev.fluid.31.1.95.

[2] W. Hogendoorn, W.-P. Breugem, D. Frank, M. Bruschewski, S. Grundmann, C. Poelma, From nearly homogeneous to core-peaking suspensions: Insights in suspension pipe flows using MRI and DNS, Phys. Rev. Fluids 8 (12) (2023) 124302, http://dx.doi.org/10.1103/PhysRevFluids.8.124302.

[3] M. Anikeeva, M. Sangal, A.N. Pravdivtsev, M.S. Pravdivtseva, E. Peschke, O. Speck, J.-B. Hövener, Magnetic resonance imaging and velocimetry of ethane, J. Magn. Reson. Open 16–17 (2023) 100137, http://dx.doi.org/10.1016/j.jmro.2023.100137.

[4] M.R. Serial, S. Benders, P. Rotzetter, D.L. Brummerloh, J.P. Metzger, S.P. Gross, J. Nussbaum, C.R. Müller, K.P. Pruessmann, A. Penn, Temperature distribution in a gas-solid fixed bed probed by rapid magnetic resonance imaging, Chem. Eng. Sci. 269 (2023) 118457, http://dx.doi.org/10.1016/j.ces.2023.118457.

[5] H. Ridder, C. Sinn, G.R. Pesch, W. Dreher, J. Thöming, Spatially resolved direct gas-phase thermometry in chemical reactors using NMR, Chem. Eng. J. 433 (2022) 133583, http://dx.doi.org/10.1016/j.cej.2021.133583.

[6] N.N. Jarenwattananon, S. Glöggler, T. Otto, A. Melkonian, W. Morris, S.R. Burt, O.M. Yaghi, L.-S. Bouchard, Thermal maps of gases in heterogeneous reactions, Nature 502 (7472) (2013) 537–540, http://dx.doi.org/10.1038/nature12568.

[7] S. Benders, F. Strassl, B. Fenger, B. Blümich, S. Herres-Pawlis, M. Küppers, Imaging of copper oxygenation reactions in a bubble flow, Magn. Reson. Chem. 56 (9) (2018) 826–830, http://dx.doi.org/10.1002/mrc.4742.

[8] D.A. Clarke, W. Hogendoorn, A. Penn, M.R. Serial, Magnetic resonance imaging in granular flows: An overview of recent advances, Particuology 101 (2025) 18–32, http://dx.doi.org/10.1016/j.partic.2023.08.007.

[9] G.H. Glover, J.M. Pauly, K.M. Bradshaw, Boron-11 imaging with a three-dimensional reconstruction method, J. Magn. Reson. Imaging 2 (1) (1992) 47–52, http://dx.doi.org/10.1002/jmri.1880020109.

[10] M. Weiger, K.P. Pruessmann, MRI with Zero Echo Time, in: EMagRes, John Wiley & Sons, Ltd, 2012, http://dx.doi.org/10.1002/9780470034590.emrstm1292.

[11] M. Weiger, K.P. Pruessmann, Short-T2 MRI: Principles and recent advances, Prog. Nucl. Magn. Reson. Spectrosc. 114–115 (2019) 237–270, http://dx.doi.org/10.1016/j.pnmrs.2019.07.001.

[12] K. Yamane, M. Nakagawa, S.A. Altobelli, T. Tanaka, Y. Tsuji, Steady particulate flows in a horizontal rotating cylinder, Phys. Fluids 10 (6) (1998) 1419–1427, http://dx.doi.org/10.1063/1.869858.

[13] M. Gromova, A. Guillermo, P.-A. Bayle, M. Bardet, In vivo measurement of the size of oil bodies in plant seeds using a simple and robust pulsed field gradient NMR method, Eur. Biophys. J. 44 (3) (2015) 121–129, http://dx.doi.org/10.1007/s00249-015-1007-z.

[14] S. Harms, S. Stapf, B. Blümich, Application of k- and q-space encoding NMR techniques on granular media in a 3D model fluidized bed reactor, J. Magn. Reson. 178 (2) (2006) 308–317, http://dx.doi.org/10.1016/j.jmr.2005.10.009.

[15] C.R. Müller, J.F. Davidson, J.S. Dennis, P.S. Fennell, L.F. Gladden, A.N. Hayhurst, M.D. Mantle, A.C. Rees, A.J. Sederman, Real-Time Measurement of Bubbling Phenomena in a Three-Dimensional Gas-Fluidized Bed Using Ultrafast Magnetic Resonance Imaging, Phys. Rev. Lett. 96 (15) (2006) 154504, http://dx.doi.org/10.1103/PhysRevLett.96.154504.

[16] M. Danczyk, T. Meaclem, M. Mehdizad, D. Clarke, P. Galvosas, L. Fullard, D. Holland, Influence of contact parameters on Discrete Element method (DEM) simulations of flow from a hopper: Comparison with magnetic resonance imaging (MRI) measurements, Powder Technol. 372 (2020) 671–684, http://dx.doi.org/10.1016/j.powtec.2020.06.002.

[17] E.E. Ehrichs, H.M. Jaeger, G.S. Karczmar, J.B. Knight, V.Y. Kuperman, S.R. Nagel, Granular Convection Observed by Magnetic Resonance Imaging, Science 267 (5204) (1995) 1632–1634, http://dx.doi.org/10.1126/science.267.5204.1632.

[18] M. Nakagawa, S.A. Altobelli, A. Caprihan, E. Fukushima, NMRI study: Axial migration of radially segregated core of granular mixtures in a horizontal rotating cylinder, Chem. Eng. Sci. 52 (23) (1997) 4423–4428, http://dx.doi.org/10.1016/S0009-2509(97)00181-4.

[19] K.M. Hill, A. Caprihan, J. Kakalios, Bulk Segregation in Rotated Granular Material Measured by Magnetic Resonance Imaging, Phys. Rev. Lett. 78 (1) (1997) 50–53, http://dx.doi.org/10.1103/PhysRevLett.78.50.

[20] A. Penn, T. Tsuji, D.O. Brunner, C.M. Boyce, K.P. Pruessmann, C.R. Müller, Real-time probing of granular dynamics with magnetic resonance, Sci. Adv. 3 (9) (2017) e1701879, http://dx.doi.org/10.1126/sciadv.1701879.

[21] M.K. Stehling, R. Turner, P. Mansfield, Echo-Planar Imaging: Magnetic Resonance Imaging in a Fraction of a Second, Science 254 (5028) (1991) 43–50, http://dx.doi.org/10.1126/science.1925560.

[22] M. Bydder, M.D. Robson, Partial fourier partially parallel imaging, Magn. Reson. Med. 53 (6) (2005) 1393–1401, http://dx.doi.org/10.1002/mrm.20492.

[23] K.P. Pruessmann, M. Weiger, M.B. Scheidegger, P. Boesiger, SENSE: Sensitivity encoding for fast MRI, Magn. Reson. Med. 42 (5) (1999) 952–962, http://dx.doi.org/10.1002/(SICI)1522-2594(199911)42:5<952::AID-MRM16>3.0.CO;2-S.

[24] A. Penn, C.M. Boyce, T. Kovar, T. Tsuji, K.P. Pruessmann, C.R. Müller, Real-Time Magnetic Resonance Imaging of Bubble Behavior and Particle Velocity in Fluidized Beds, Ind. Eng. Chem. Res. 57 (29) (2018) 9674–9682, http://dx.doi.org/10.1021/acs.iecr.8b00932.

[25] A. Penn, C.M. Boyce, K.P. Pruessmann, C.R. Müller, Regimes of jetting and bubbling in a fluidized bed studied using real-time magnetic resonance imaging, Chem. Eng. J. 383 (2020) 123185, http://dx.doi.org/10.1016/j.cej.2019.123185.

[26] J.P. Metzger, B. Chen, A. Penn, C. Guenthner, K.P. Pruessmann, C.R. Müller, Magnetic resonance velocimetry of particle hydrodynamics in a three-dimensional draft tube spout-fluid bed, Chem. Eng. J. 485 (2024) 149678, http://dx.doi.org/10.1016/j.cej.2024.149678.

[27] E.M. Haacke, R.W. Brown, M.R. Thompson, R. Venkatesan, Magnetic Resonance Imaging, John Wiley & Sons, 1999.

[28] D.P. Burum, W.K. Rhim, Analysis of multiple pulse NMR in solids. III, J. Chem. Phys. 71 (2) (1979) 944–956, http://dx.doi.org/10.1063/1.438385.

[29] J.F. Schenck, The role of magnetic susceptibility in magnetic resonance imaging: MRI magnetic compatibility of the first and second kinds, Med. Phys. 23 (6) (1996) 815–850, http://dx.doi.org/10.1118/1.597854.

[30] M.E. Stoll, T.J. Majors, Reduction of magnetic susceptibility broadening in NMR by susceptibility matching, J. Magn. Reson. (1969) 46 (2) (1982) 283–288, http://dx.doi.org/10.1016/0022-2364(82)90143-3.

[31] S. Gross, C. Barmet, B.E. Dietrich, D.O. Brunner, T. Schmid, K.P. Pruessmann, Dynamic nuclear magnetic resonance field sensing with part-per-trillion resolution, Nat. Commun. 7 (1) (2016) 13702, http://dx.doi.org/10.1038/ncomms13702.

[32] C. Barmet, Spatiotemporal Magnetic Field Monitoring for Magnetic Resonance Systems (Ph.D. thesis), ETH Zürich, 2008.

[33] R.S. Davis, Equation for the volume magnetic susceptibility of moist air, Metrologia 35 (1) (1998) 49, http://dx.doi.org/10.1088/0026-1394/35/1/8.

[34] B. Partopour, A.G. Dixon, An integrated workflow for resolved-particle packed bed models with complex particle shapes, Powder Technol. 322 (2017) 258–272, http://dx.doi.org/10.1016/j.powtec.2017.09.009.
[35] B. Partopour, A.G. Dixon, Effect of particle shape on methanol partial oxidation in a fixed bed using CFD reactor modeling, AIChE J. 66 (5) (2020) e16904, http://dx.doi.org/10.1002/aic.16904.
[36] J.D. Jackson, Classical Electrodynamics (Third Edition), John Wiley & Sons, 1999.
[37] J. Blahovec, Mechanics of Poppy Seeds, Int. J. Food Prop. 5 (2) (2002) 277–287, http://dx.doi.org/10.1081/JFP-120005785.
[38] C.M. Boyce, A. Penn, K.P. Pruessmann, C.R. Müller, Magnetic resonance imaging of gas–solid fluidization with liquid bridging, AIChE J. 64 (8) (2018) 2958–2971, http://dx.doi.org/10.1002/aic.16036.
[39] S. Aime, M. Botta, L. Barbero, F. Uggeri, F. Fedeli, Water signal suppression by T2-relaxation enhancement promoted by Dy(III) complexes, Magn. Reson. Chem. 29 (13) (1991) S85–S88, http://dx.doi.org/10.1002/mrc.1260291316.
[40] K.E. Kellar, S.L. Fossheim, S.H. Koenig, Magnetic Field Dependence of Solvent Proton Relaxation by Solute Dysprosium(III) Complexes, Invest. Radiol. 33 (11) (1998) 835.
[41] J. Vymazal, J.W.M. Bulte, J.A. Frank, G.D. Chiro, R.A. Brooks, Frequency dependence of MR relaxation times I. Paramagnetic ions, J. Magn. Reson. Imaging 3 (4) (1993) 637–640, http://dx.doi.org/10.1002/jmri.1880030413.